EPJ Applied Metamaterials

RESEARCH ARTICLE

OPEN ACCESS

Negative index and mode coupling in all-dielectric metamaterials at terahertz frequencies

Eric Akmansoy[1,2,*] and Simon Marcellin[1,2]

[1] Institut d'Electronique Fondamentale, Univ. Paris-Sud, Universite Paris-Saclay, 91405 Orsay, France
[2] UMR 8622, CNRS, 91405 Orsay, France

Abstract. We elucidate the role of the mode coupling of the Mie resonances in all-dielectric metamaterials to ensure a negative effective index at terahertz frequencies. We perform a study as a function of the lattice period and of the frequency overlapping of the modes of resonance. We show that negative effective refractive index requires sufficiently strong mode coupling and that for even more strong mode coupling, the first two modes of Mie resonances are degenerate; the effective refractive index is then undetermined. We also show that it is possible to obtain near-zero, or even null, effective index with a judicious adjustment of the mode coupling. Further, we discuss the mode coupling effect with hybridization in metamaterials.

Keywords: All-dielectric metamaterials / Negative index / Mode coupling / Near-zero refractive index

1 Introduction

All-dielectric metamaterials (ADMs) are the promising "inflection" of metamaterials to go beyond their limits. ADMs are an alternative to metallic metamaterials. The advantages of ADMs come from their low losses and their simple geometry: they do not suffer from Ohmic losses and thus they may benefit from low energy dissipation, specially, ceramics of high dielectric permittivity and high quality factor [1,2]. In the microwave, their quality factor is greater than that of metallic metamaterials [3], and it is consequently also the case in terahertz (THz) and optical frequencies. ADMs are partly inspired by the work of Richtmyer who developed the theory of dielectric resonators, which is based on the fact that "the dielectric has the effect of causing the electromagnetic field [. . .] to be confined to the cylinder itself and the immediately surrounding region of space" [4]. Taking the matter further, O'Brien and Pendry opened the way for ADMs by considering the periodic lattice of high permittivity resonators (HPRs), thus demonstrating artificial magnetism in the microwave [2,5]. ADMs rely on the first two modes of the Mie resonances of HPR. The first mode results in resonant effective permeability that can have negative values, while the second one results in resonant effective permittivity that can also have negative values. When both are simultaneously negative, the ADM is called "double negative" (DNG) and its effective refractive index is then

negative [6–11]. The unit cell of ADM thus comprises two subwavelength building blocks of simple geometry [12,13]. In analogy with chemical molecules, the unit cell is generally called a *meta-dimer* [14], and the two building blocks are called *meta-atoms*. As the two are different, the unit cell is a hetero-dimer.

The large applications of ADMs (for a review, see Ref. [15]) include perfect reflectors [16], perfect absorbers [17,18], zero-index metamaterials [19], optical magnetic mirror [20], and Fano resonances [21,22]. ADMs have been demonstrated from the microwave to the optical domain. Artificial magnetism [3,23–25] and negative effective refractive index [26,27] have been, theoretically and experi-mentally, shown in the GHz regime. Even though artificial magnetism provided by ADMs has been experimentally demonstrated in the THz [28] and infrared ranges [29–32], DNG refractive index has not been yet demonstrated, which impedes ADMs to be the equivalent of their metallic counterpart. Besides, THz radiation is widely defined as electromagnetic radiation in the frequency range 0.3–3 THz. It permits the obtention of physical data that are not accessible using X-ray or infrared radiation and it thus finds many applications in imaging, security, quality inspection, chemical sensing, astronomy, etc. On their part, metamaterials have evolved towards the implementation of photonic components [33]. HPRs are well suited for metamaterial applications in the low THz frequency range [34].

In the following, we report on the mode coupling effect which plays a dominant role in the electromagnetic properties of metamaterials [35–39], notably, in the achievement of a negative effective index. Magnetic and
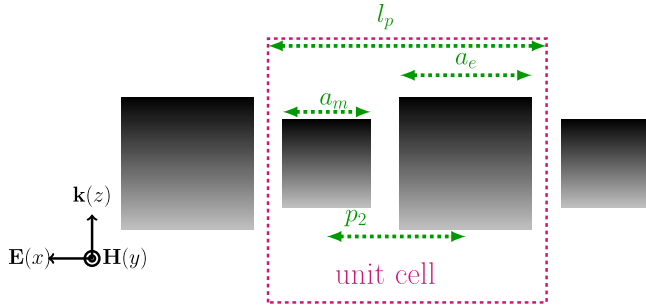
---

* e-mail: eric.akmansoy@u-psud.fr

Fig. 1. Schematic layout of the 2D ADM (cross-sectional view). The ADM consists of one infinite layer along the x direction and is made up of two interleaved sets of high permittivity square cross-section dielectric cylinders, which resonate in the first two modes of Mie resonances: the small set resonates in the *magnetic* mode and the second one in the *electric* mode. The equidistant cylinders are infinite along the y direction and their side lengths are $a_m = 60\,\mu\text{m}$ and $a_e = 90\,\mu\text{m}$, respectively. Their relative permittivity is $\epsilon_r = 94$. The unit cell actually consists of two subwavelength distinct building blocks. The lattice period is $l_p = 260\,\mu\text{m}$ and p_2 is half the lattice period. The incident wave is transverse electric (TE).

electric mode coupling effects in ADMs have been separately studied in the microwave by Zhang *et al.* [36]. Herein, we report on the magneto-electric mode coupling effects in the THz domain, and we show that negative effective refractive index requires sufficiently strong mode coupling [40]. We also show that adjusting the mode coupling allows us to attain near-zero values of the refractive index, or even null effective index. Moreover, we highlight that the strongest values of the mode coupling lead to frequency mode degeneracy, for which the refractive index is undetermined.

2 Simulations

We consider a 2D ADM whose unit cell consists of two distinct building blocks, a *magnetic* block and an *electric* one, the former resonating in the first mode of Mie resonances and the latter resonating in the second mode [3,13,27,41]. The first mode is thus referred to as the *magnetic* mode and the second one as the *electric* mode. The ADM consists of one infinite layer made up of two sets of high permittivity square cross-section dielectric cylinders that are perpendicular to the incident wave vector (Fig. 1). The two sets of infinitely long HPRs are actually interleaved. The incident polarization is transverse electric (TE), i.e., the electric field is perpendicular to the axis of the cylinders. We studiy both *spatial* mode coupling and *frequency* mode coupling. The ADM has been numerically simulated by the means of the finite elements method software HFSS$^{\text{TM}}$, which yields the S-parameters. The side lengths of the resonators are initially $a_m = 60\,\mu\text{m}$ for the magnetic mode and $a_e = 90\,\mu\text{m}$ for the *electric* one, while the lattice period is $l_p = 260\,\mu\text{m}$. The HPRs are equidistant and therefore, the distance between two of them is half the lattice period $p_2 = l_p/2 = 130\,\mu\text{m}$. The relative permittivity of the

dielectric is $\epsilon_r = 94$ (titanium dioxide $-$ TiO$_2$) and the loss tangent increases between $\tan \delta = 0.009$ and 0.015 in the considered frequency range [42,43]. We are thus dealing with a high refractive index bulk material ($N_{\text{TiO}_2} \simeq 10$).

3 Results and discussion

3.1 Negative index and mode coupling

We study the mode coupling between the first two modes of Mie resonances depending on the lattice period l_p (*spatial* mode coupling), and then depending on the frequency overlapping of the two modes (*frequency* mode coupling). The results of the simulation, namely the minimum $n_{\text{eff}_{\text{min}}}$ of the real part of the effective index n_{eff} as a function of the lattice period and as a function of the frequency spacing between the two modes, are reported in Figures 2 and 3, respectively. They show that the mode coupling should be strong enough to ensure negative effective index. The minima of the real part of the effective index n_{eff} are $n_{\text{eff}_{\text{min}}} = -2.2$ and -1.9, respectively. On the one hand, increasing the mode coupling is obtained by decreasing the lattice period l_p. On the other hand, it is obtained by decreasing the frequency of the second mode of Mie resonances, which stems from the increasing of the side length a_e of the *electric* resonator. When the mode coupling is sufficient, the bandwidth of the negative effective index n_{eff} increases with it (see insets in Figs. 2 and 3). The frequency range of negative effective index is given by the relation [44]

$$\epsilon'(\omega)\cdot\mu''(\omega) + \epsilon''(\omega)\cdot\mu'(\omega) \leq 0, \tag{1}$$

where $'$ and $''$ respectively denote the real and imaginary parts of the permeability μ and the permittivity ϵ.

3.2 Monomode coupling

To carry out our study, we first explored monomode coupling, that is, the mode coupling due to only one mode, which arises inside a layer whose unit cell only consists of one building block, the *magnetic* one or the *electric* one. We study both cases. Consequently, we only consider the *spatial* mode coupling and only varied the lattice period l_p which is equal to the distance p_1 between two resonators, $l_p = p_1$. Operating in the same frequency range, the side length of the *magnetic* resonator is $a_m = 60\,\mu\text{m}$, while that of the *electric* resonator is $a_e = 90\,\mu\text{m}$. The results of the simulation are reported in Figures 4 and 5, for both cases, and they show that the two modes behave differently. Their respective frequencies (f_{mr}, f_{er}) are given by the minima of the S_{12} parameter [36]. The frequency f_{mr} of the *magnetic* mode increases with the lattice period l_p, whereas the frequency f_{er} of the *electric* one decreases. These results are consistent with that of Zhang et al [36]. Both maxima of the absorption A_{mr} and A_{er} ($A(\omega) = 1 - |S_{12}(\omega)|^2 - |S_{11}(\omega)|^2$) and the frequency of the resonance modes of the individual resonator are also reported. The latter provides a series of resonances whose frequency is
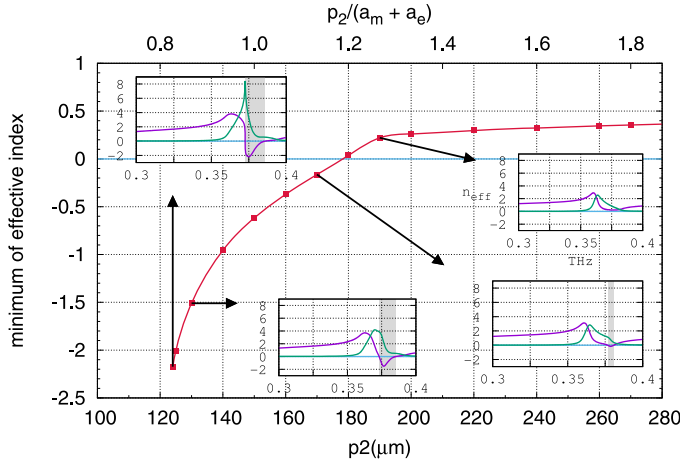
Fig. 2. *Spatial* mode coupling: minimal value of the effective refractive index n_{eff} as a function of the distance p_2 between the two resonators. The side lengths of the resonators are $a_m = 60\,\mu\mathrm{m}$ and $a_e = 90\,\mu\mathrm{m}$, respectively. Insets: real (purple) and imaginary part (green) of the effective index n_{eff}; the shaded area denotes the bandwidth of negative effective index.
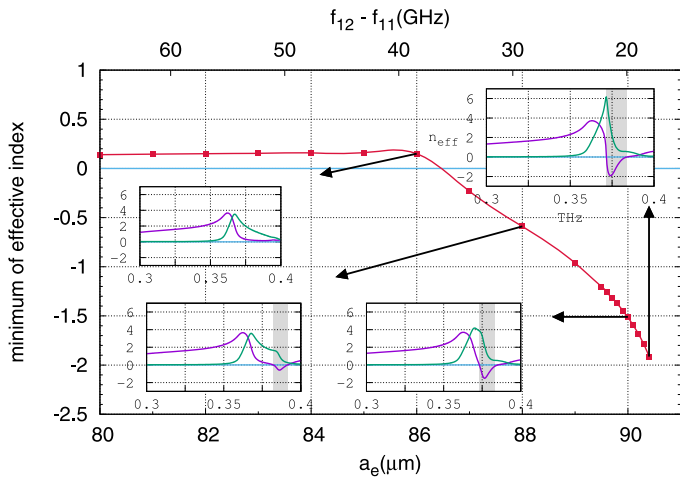

Fig. 4. *Magnetic* mode coupling: frequency (f_{mr}) of the first mode of Mie resonances and of the maximum of absorption (A_{mr}) as a function of the distance p_1 between two resonators. The unit cell only comprises the *magnetic* block. The side length of the resonator is $a_m = 60\,\mu\mathrm{m}$. The dashed line denotes the resonance frequency (f_{11}) of the mode of resonances of the individual resonator.

Fig. 3. *Frequency* mode coupling: minimal value of the effective refractive index n_{eff} as a function of the side length a_e of the *electric* resonator, namely, the frequency of the *electric* mode is varying. Insets: real (purple) and imaginary part of (green) the effective index n_{eff}; the shaded area denotes the bandwidth of negative effective index. f_{11} and f_{12} are the resonances frequencies of the individual resonators (see the text).

Fig. 5. *Electric* mode coupling: frequency (f_{er}) of the second mode of Mie resonances and of the maximum of absorption (A_{er}) as a function of the distance p_1 between two resonators. The unit cell only comprises the *electric* block. The side length of the resonator is $a_e = 90\,\mu\mathrm{m}$. The dashed line denotes the resonance frequency (f_{12}) of the mode of resonances of the individual resonator.

determined by Cohn's model [1,26,45,46].

$$f_{mn} = \frac{c}{2\sqrt{\epsilon_r}}\sqrt{\left(\frac{m}{a}\right)^2 + \left(\frac{n}{b}\right)^2},\tag{2}$$

where ϵ_r is the relative permittivity of the resonator, m and n the integers, a and b the side lengths of the resonator, and c is the velocity of light and its accuracy is about 5%. Equation 2 was used to design all the reported structures. For a square cross-section cylinder, $a = b$, and the frequencies of the first two modes of the individual resonator respectively correspond to $m = n = 1$ and $m = 1$
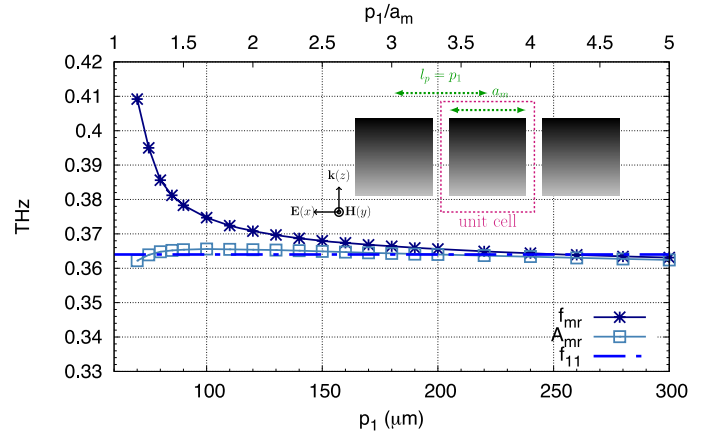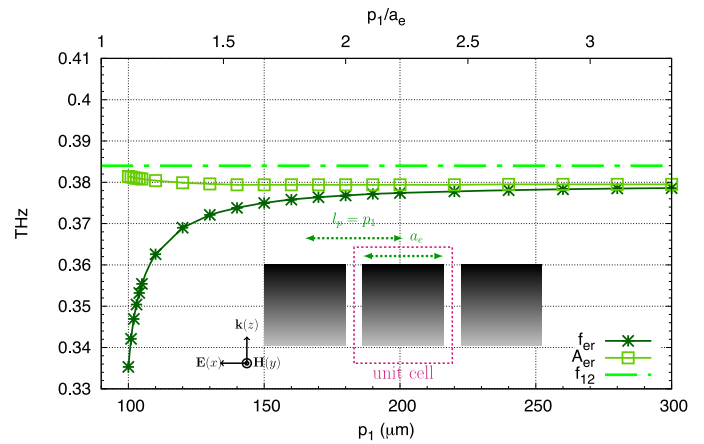
and $n = 2$. To exhibit negative refractive index, the involved resonance modes are the first mode of the magnetic resonator and the second mode of the electric resonator. Their frequencies are respectively $f_{11} = 0.364$ THz ($a = a_m = 60\,\mu\mathrm{m}$) and $f_{12} = 0.384$ THz ($a = a_e = 90\,\mu\mathrm{m}$) [27]. These are obviously constant, while the maxima of the absorption are nearly constant. It can be noticed that, as the mode coupling increases, the distance between the resonance frequencies (f_{mr}, f_{er}) of the resonator inside the layer and that (f_{11}, f_{12}) of the individual resonator respectively increases (cf. Figs. 4 and 5, respectively), thus demonstrating the mode coupling.
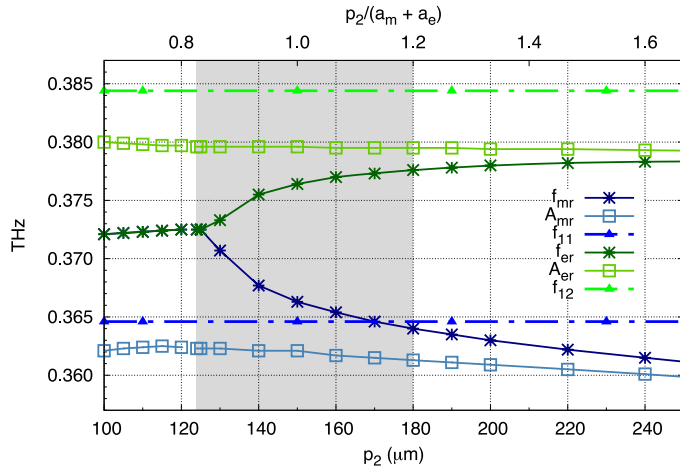
Fig. 6. *Spatial* mode coupling: frequency of the first two modes of Mie resonances as a function of the distance p_2 between two resonators which is half the lattice period l_p. Blue and green colors denote the *magnetic* and the *electric* modes, respectively. Square dots and crossed dots denote the maxima of absorption (A_{mr}, A_{er}) and the minimum of the S_{12} parameter (f_{mr}, f_{er}), respectively. The shaded area corresponds to negative value of the effective index n_{eff}. The side lengths of both resonators are $a_m = 60\,\mu$m and $a_e = 90\,\mu$m, respectively. The dashed lines denote the frequencies of resonances (f_{11}, f_{12}) of the modes of the individual resonator.

3.3 Bimodal coupling

We next explore the mode coupling inside the ADM, namely, the unit cell now consists of the two building blocks. The variation of the resonance frequencies (f_{mr}, f_{er}) of both modes is reported in Figures 6 and 7 corresponding to the *spatial* mode coupling and the *frequency* mode coupling, respectively. These frequencies are still given by the minima of the S_{12} parameter [36]. Decreasing the lattice period l_p, i.e., the distance p_2 between the resonators, increases the mode coupling. Varying the overlapping of the two modes stems from the decreasing of the frequency of the *electric* mode, which also increases the mode coupling [35]. The curves are shaped as "tuning forks" and show that the frequencies (f_{mr}, f_{er}) of the two modes of resonance are moving closer together as the mode coupling increases. To highlight this effect, the frequencies (f_{11}, f_{12}) of the resonance modes of the individual resonator are again shown in these figures. For both the *magnetic* mode and the electric one, the distance between the frequency (f_{mr}, f_{er}) of the resonator inside the ADM and the frequency (f_{11}, f_{12}) of the individual one respectively increases as the mode coupling increases. This anew evidences the mode coupling inside the ADM. Theses curves also show that further increasing the mode coupling gives rise to a frequency degeneracy in both cases of mode coupling, that is, the two resonance frequencies of the two modes become equal, $f_{mr} = f_{er}$.

The S_{12} parameter and the absorption A are reported in Figure 8 as a function of frequency for several values of lattice period l_p, which is relative to the *spatial* mode coupling. Two ranges of lattice period l_p are considered, one is out of the frequency degeneracy regime ($250 \leq l_p \leq$
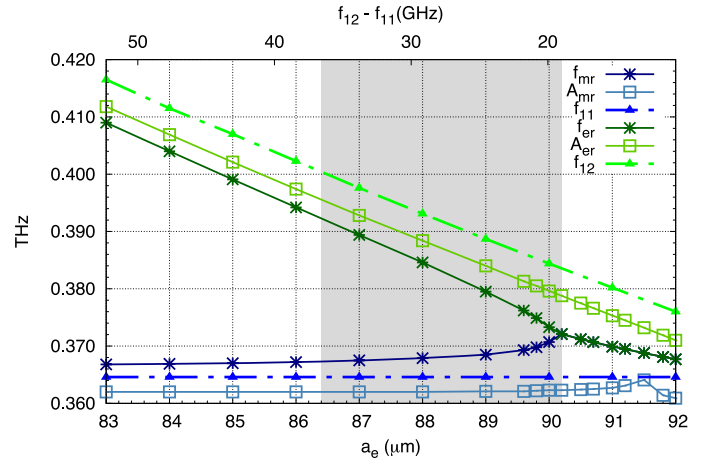

Fig. 7. *Frequency* mode coupling: frequency of the first two modes of Mie resonances (f_{mr}, f_{er}) as a function of the side length a_e of the *electric* resonator, namely, the frequency of the *electric* mode is varying. The convention is the same as in Figure 6. The side length of the *magnetic* resonator is $a_m = 60\,\mu$m and the lattice period l_p is 260 μm.

$400\,\mu$m) and the second one in the frequency degeneracy regime ($200 \leq l_p \leq 248\,\mu$m). It can be noticed that the frequency of both maxima of absorption are practically constant, whereas the frequency of both minima of the S_{12} parameter vary with the lattice period l_p. The latter move closer together as the lattice period l_p increases, until they merged, which corresponds to the frequency degeneracy. The crossing point is reached when the lattice period is equal to $l_{pc} = 250\,\mu$m. The merged minima of the S_{12} parameter are very weak ($\lesssim -51$dB) for $l_p = 248\,\mu$m, which corresponds to the minimum of the real part of the effective index $n_{eff_{min}}(l_p = 248\,\mu$m$) = -2.2$. (See effective index curves inserted in Figs. 2 and 3 which are continuous, but at the limit of continuity.) For greater values of the mode coupling, that is, for lattice period l_p smaller than $248\,\mu$m, the effective parameters could not be extracted, being not continuous through all frequencies [47]; the effective refractive index n_{eff} is then undetermined. We observed the same frequency degeneracy behavior when studying the *frequency* mode coupling (results not shown).

The mode coupling effect we report here is different from hybridization [48] which is observed with plasmonic metameterial [14,49], split-ring resonators metametarials [50], inductor-capacitor resonators [51], cut wires [52], nano-wires [53], nano-rings [54], nano-particle dimers [55], or silicon nanoparticles [56]. In these cases, the coupling between the two identical meta-atoms which constitute the dimer leads from a trapped mode to the formation of new hybridized modes because it lifts the degeneracy of the mode of the individual meta-atoms. Hybridization may be used to yield negative refractive index [50,51,54]. The unit cell is then a homo-dimer and the negative effective index is achieved by playing with the mode coupling so as to overlap two hybridized modes which are of different kind: *magnetic* or *electric*. In the case we report here, the mechanism is different since it takes the reverse way,
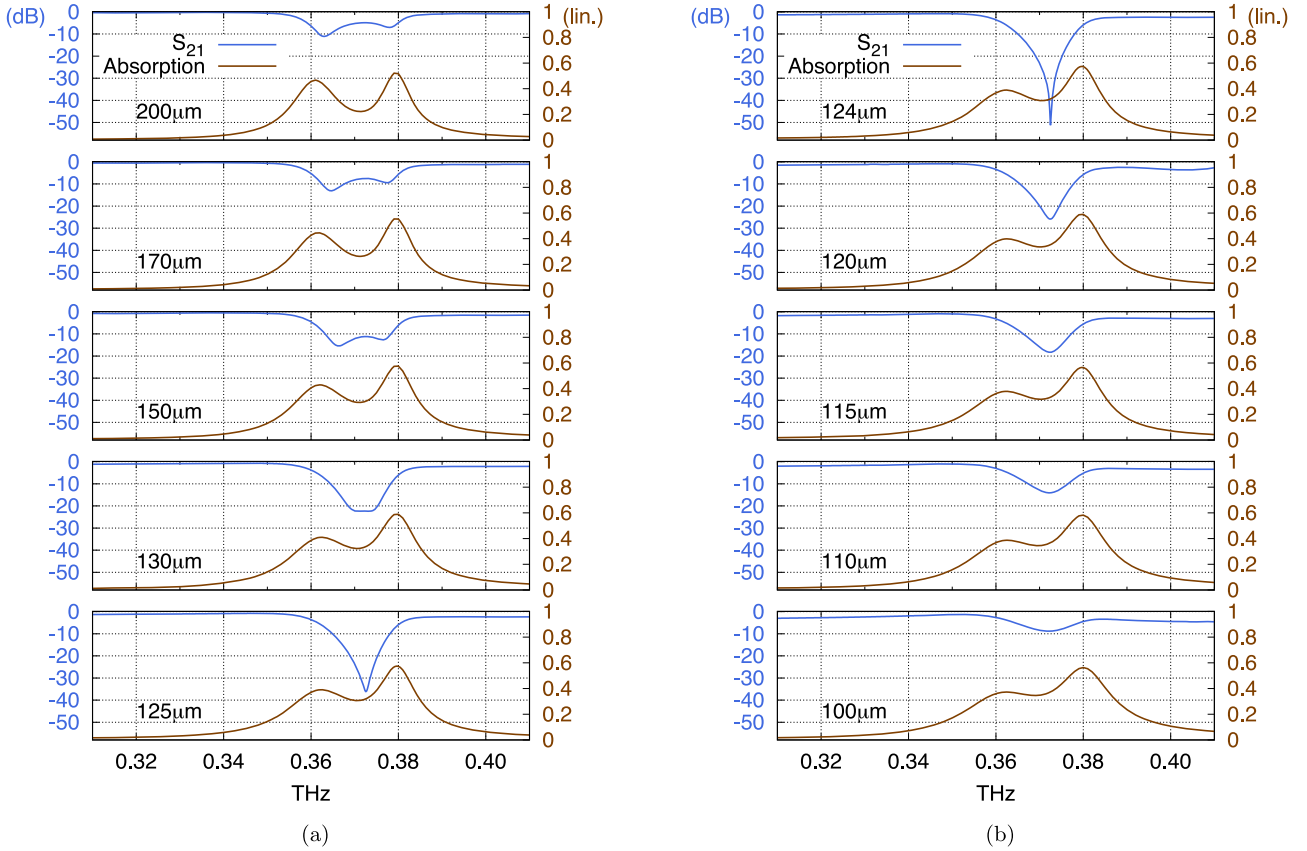
(a)   (b)

Fig. 8. Effect of *spatial* mode coupling: S_{12} parameter (log. scale (dB)) and absorption A (linear scale (lin.)) for several values of distance p_2 between two resonators. The side lengths of the resonators are $a_m = 60\,\mu\mathrm{m}$ and $a_e = 90\,\mu\mathrm{m}$. (a) Out of frequency degeneracy regime ($125 \leq p_2 \leq 200\,\mu\mathrm{m}$); (b) in frequency degeneracy regime ($100 \leq p_2 \leq 124\,\mu\mathrm{m}$). The merged minima of the S_{12} parameter attain very weak values ($\lesssim -51\,\mathrm{dB}$) when $p_2 = p_{2c} = 124\,\mu\mathrm{m}$, which correspond to the minimum of the refractive index $n_{\mathrm{eff}_{\min}} = -2.2$.

because increasing the mode coupling leads from two separate modes to a trapped one. The unit cell of our ADM is a hetero-dimer because the two meta-atoms are not identical, and moreover, each one resonates in a different kind of mode: the *magnetic* one and the *electric* one. Hence, increasing the mode coupling leads to the trapped mode putting together the two separate modes. Nevertheless, the mode coupling has to be strong enough to ensure a negative effective index, the unit cell being either a homo-dimer or a hetero-dimer.

3.4 Effective parameters

In our ADM, a *magnetic* moment ensues from the *magnetic* mode giving rise to resonant effective permeability μ_{eff}. Similarly, an *electric* moment ensues from the electric mode giving rise to resonant effective permittivity ϵ_{eff}. The two are perpendicular to each other (see e.g., Fig. 1 in reference [41]). The mode coupling arises from the interaction between these electromagnetic moments and it changes with the separating distance. The side lengths of the resonators are afresh $a_m = 60\,\mu\mathrm{m}$ and $a_e = 90\,\mu\mathrm{m}$. Both resonances consequently modify the effective refractive index $n_{\mathrm{eff}}(\omega)$ of the ADM. The effective electromagnetic parameters μ_{eff}, ϵ_{eff} and n_{eff} are reported in Figure 9 relative

to two values of the lattice period $l_p = 360\,\mu\mathrm{m}$ and $l_p = 260\,\mu\mathrm{m}$. They are extracted from the S-parameters using the common retrieval method described in references [47,57–63]. The antiresonance behavior of the effective permittivity e_{eff} around the *magnetic* mode frequency, which is inherent in metamaterials, can be observed [62–65]. In the former case (low mode coupling), the real part of the effective index n_{eff} does not reach negative values, whereas it does in the latter case (strong mode coupling), then satisfying equation 1. The minimum value of the real part of the effective index is then $n_{\mathrm{eff}_{\min}}(l_p = 260\,\mu\mathrm{m}) = -1.5$. In the former case, the real part of the effective index n_{eff} is below unity and close to zero. Its minimal value is $n_{\mathrm{eff}_{\min}}(l_p = 360\,\mu\mathrm{m}) \lesssim 0.04$, demonstrating that adjusting the mode coupling makes ADMs suitable for epsilon-near-zero (ENZ) metamaterials [66,67] (see also Fig. 2), or even null effective index [19]. It can also be noticed that the mode coupling strongly enhances the amplitude of both resonances, notably the *electric* one, and that it brings closer together the two modes. In addition, as we are dealing with a high refractive index bulk material ($N_{\mathrm{TiO_2}} \simeq 10$), the wavelength inside it is about one-tenth of that in vacuum. Consequently, we calculated the static effective permittivity, i.e., beyond the resonances, from the Maxwell–Garnett model [68]. It is equal to $\epsilon_{\mathrm{eff}} = 2.1$ and $\epsilon_{\mathrm{eff}} = 2.9$ corresponding to both values of the lattice period
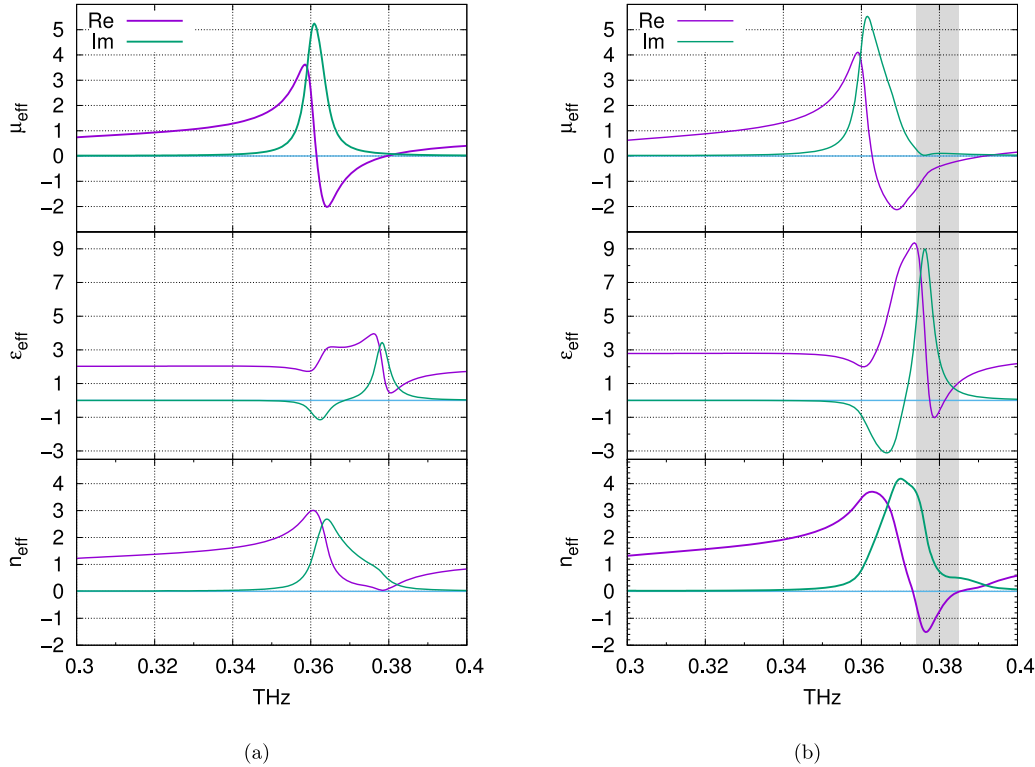
(a)   (b)

Fig. 9. Effect of *spatial* mode coupling: effective electromagnetic parameters (real and imaginary parts): permeability μ_{eff} (top), permittivity ϵ_{eff} (middle) and effective index n_{eff} (bottom). (a) Low mode coupling: lattice period $l_p = 360\,\mu$m: the minimum value of the effective refractive index is $n_{\mathrm{eff_{min}}} < 0.04$; (b) strong mode coupling: lattice period $l_p = 260\,\mu$m. The shaded area denotes the bandwidth of the negative effective index: the minimum value of the effective refractive index is $n_{\mathrm{eff_{min}}} = -1.5$. The static effective permittivity values yielded by the Maxwell–Garnett formula, $\epsilon_{\mathrm{eff}} = 2.1$ and $\epsilon_{\mathrm{eff}} = 2.9$, are in good agreement with the result of the simulation.
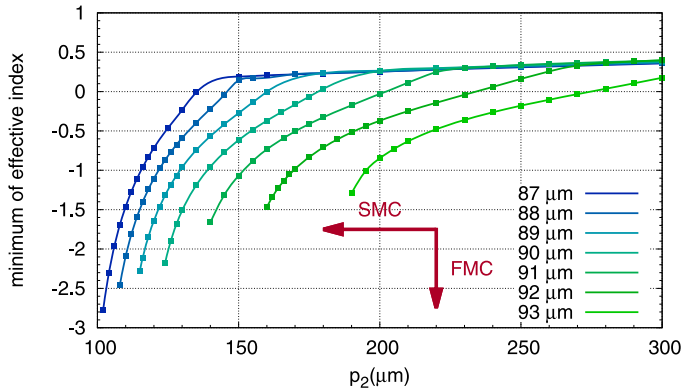

Fig. 10. Effect of both mode couplings (*spatial* mode coupling (SMC) and frequency mode coupling (FMC)): minimal value of the effective refractive index n_{eff} as a function of the distance p_2 between two resonators for several values of the side length a_e of the *electric* resonator. The side length of the *magnetic* resonator is $a_m = 60\,\mu$m. The two arrows denote increasing mode coupling. The minimum of the real part of the effective index is $n_{\mathrm{eff_{min}}} = -2.8$.

$l_p = 360\,\mu$m and $l_p = 260\,\mu$m, respectively, which is in good agreement with the results of the simulation (see Fig. 9a and b-middle).

To engineer the electromagnetic properties of an ADM, one can consequently play with either mode couplings:

the *spatial* mode coupling or the *frequency* mode coupling. Figure 10 gathers the role of both mode couplings: the stronger the two mode couplings, the more negative the effective index and the larger the bandwidth of negative effective index (cf. Figs. 2 and 3). Combining the two mode couplings, negative effective index as low as $n_{\mathrm{eff}} = -2.8$ is obtained.

3.5 Dielectric function, phonons and strontium titanate (SrTiO₃)

Other high permittivity materials, having low losses, can be investigated to study the mode coupling inside ADMs at THz frequencies, e.g., $SrTiO_3$ [69–72]. However, the dielectric function $\epsilon_r(\omega)$ of these high permittivity materials is dispersive, because of lattice vibrations, namely, due to optical phonons [73]. Their frequency is in the THz range, and we are concerned with the transverse optical phonon of lowest frequency (TO₁). The TO₁ phonon frequency of $SrTiO_3$ is 2.70 THz [69], while that of TiO_2 is 5.6 THz [69,73]. The dielectric function $\epsilon_r(\omega)$ is described by the classical oscillator model or the Four-Parameter Semi Quantum (FPSQ) model [69,71,73]. Measurements in the THz frequency, reported in the literature, are in good agreement with these models for TiO_2 [42,43] and $SrTiO_3$ [71,72,74,75]. The two yield the same dielectric function $\epsilon_r(\omega)$ at the operating frequency.

The latter also reflect that the imaginary part of the dielectric function $\epsilon_r(\omega)$ strongly increases around the frequency of the TO_1 phonon. We also simulated a similar ADM but consisting of HPRs made of $SrTiO_3$ and found that it exhibits the same mode coupling effects (results not shown here). The real part of the effective index reaches values as low as $n_{eff_{min}} = -7$, meaning that the effect of the mode coupling is stronger when a higher permittivity material is used ($\epsilon_r \simeq 300$ [72] as compared with $\epsilon_r = 94$), because this heightens the resonances.

However, losses (imaginary part of $\epsilon_r(\omega)$) resulting from the TO_1 phonon greatly increase and therefore limit the operating range at THz frequencies. In addition, the real part of the dielectric function $\epsilon_r(\omega)$ falls down at higher frequency [72,74], which drastically modifies the Mie resonances. The lower permittivity of TiO_2 leads to greater side lengths a_m and a_e of each resonator (see Eq. (2)) and therefore, it facilitates their fabrication. Consequently, TiO_2 is more suitable for ADM applications at THz frequencies.

4 Conclusion

We have studied mode coupling effects in ADMs at THz frequencies, and we show that the mode coupling has to be sufficiently strong to ensure negative effective index of refraction. Tuning the first two modes of Mie resonances of an ADM by adjusting the mode coupling allows the setting of the effective index from a near-zero value to a negative value. We studied both spatial mode coupling and frequency mode coupling. Increasing both brings the modes closer together until they are merged. Thus, we highlight the frequency degeneracy of the first two resonance modes, namely, the two frequencies are equal, and the effective index is then undetermined. At the crossing point, the effective index reaches its lowest value.

Author contribution statement

E.A. supervised the study, analyzed the results and wrote the paper. S.M. made the simulation and analyzed the results.

References

1. D. Kajfez, P. Guillon, Dielectric Resonators, (Artech House, Dedham, MA, 1986)
2. S. Fiedziuszko, I. Hunter, T. Itoh, Y. Kobayashi, T. Nishikawa, S. Stitzer, K. Wakino, Dielectric materials, devices, and circuits, IEEE Trans. Microw. Theory Tech. **50**, 706 (2002)
3. B.-I. Popa, S.A. Cummer, Compact dielectric particles as a building block for low-loss magnetic metamaterials, Phys. Rev. Lett. **100**, 207401 (2008)
4. R.D. Richtmyer, Dielectric resonators, J. Appl. Phys. **10**, 391 (1939)
5. S. O'Brien, J.B. Pendry, Photonic band-gap effects and magnetic activity in dielectric composites, J. Phys.: Condens. Matter **14**, 15 (2002)
6. J.B. Pendry, D.R. Smith, Reversing light with negative refraction, Phys. Today **57**, 37 (2004)
7. W.J. Padilla, D.N. Basov, D.R. Smith, Negative refractive index metamaterials, Mater. Today **9**, 28 (2006)
8. D.R. Smith, W.J. Padilla, D.C. Vier, S.C. Nemat-Nasser, S. Schultz, Composite medium with simultaneously negative permeability and permittivity, Phys. Rev. Lett. **84**, 4184 (2000)
9. R.W. Ziolkowski, Design, fabrication, and testing of double negative metamaterials, IEEE Trans Antenn Propag. **51**, 1516 (2003)
10. N. Engheta, R.W. Ziolkowski, A positive future for double-negative metamaterials, IEEE Trans. Microw. Theory Tech. **53**, 1535 (2005)
11. R. Liu, A. Degiron, J.J. Mock, D.R. Smith, Negative index material composed of electric and magnetic resonators, Appl. Phys. Lett. **90**, 263504 (2007)
12. A. Ahmadi, H. Mosallaei, Physical configuration and performance modeling of all-dielectric metamaterials, Phys. Rev. B **77**, 045104 (2008)
13. Q. Zhao, J. Zhou, F. Zhang, D. Lippens, Mie resonance-based dielectric metamaterials, Mater. Today **12**, 60 (2009)
14. N. Liu, H. Liu, S. Zhu, H. Giessen, Stereometamate-rials, Nat. Photonics **3**, 157 (2009)
15. S. Jahani, Z. Jacob, All-dielectric metamaterials, Nat Nano **11**, 23 (2016)
16. P. Moitra, B.A. Slovick, W. Li, I.I. Kravchencko, D.P. Briggs, S. Krishnamurthy, J. Valentine, Large-scale all-dielectric metamaterial perfect reflectors, ACS Photonics **2**, 692 (2015)
17. X. Liu, Q. Zhao, C. Lan, J. Zhou, Isotropic mie resonance-based metamaterial perfect absorber, Appl. Phys. Lett. **103**, 031910 (2013)
18. X. Liu, K. Bi, B. Li, Q. Zhao, J. Zhou, Metamaterial perfect absorber based on artificial dielectric "atoms", Opt. Express **24**, 20454 (2016)
19. P. Moitra, Y. Yang, Z. Anderson, I.I. Kravchenko, D.P. Briggs, J. Valentine, Realization of an all-dielectric zero-index optical metamaterial, Nat. Photon. **7**, 791 (2013)
20. S. Liu, M.B. Sinclair, T.S. Mahony, Y.C. Jun, S. Cam-pione, J. Ginn, D.A. Bender, J.R. Wendt, J.F. Ihlefeld, P.G. Clem, J.B. Wright, I. Brener, Optical magnetic mirrors without metals, Optica **1**, 250 (2014)
21. B. Luk'yanchuk, N.I. Zheludev, S.A. Maier, N.J. Ha-las, P. Nordlander, H. Giessen, C.T. Chong, The fano resonance in plasmonic nanostructures and metama-terials, Nat. Mater. **9**, 707 (2010).
22. T. Lepetit, E. Akmansoy, J.-P. Ganne, J.-M. Lour-tioz, Resonance continuum coupling in high-permittivity dielectric metamaterials, Phys. Rev. B **82**, 195307 (2010)
23. Q. Zhao, L. Kang, B. Du, H. Zhao, Q. Xie, X. Huang, B. Li, J. Zhou, L. Li, Experimental demonstration of isotropic negative permeability in a three-dimensional dielectric composite, Phys. Rev. Lett. **101**, 027402 (2008)
24. T. Lepetit, E. Akmansoy, M. Pate, J.P. Ganne, Broadband negative magnetism from all-dielectric meta-material, Electron. Lett. **44**, 1119 (2008)
25. I. Vendik, M. Odit, D. Kozlov, 3D isotropic metama-terial based on a regular array of resonant dielectric spherical inclusions, Metamaterials **3**, 140 (2009)

26. J. Kim, A. Gopinath, Simulation of a metamaterial containing cubic high dielectric resonators, Phys. Rev. B **76**, 115126 (2007)

27. T. Lepetit, E. Akmansoy, J.-P. Ganne, Experimental measurement of negative index in an all-dielectric meta-material, Appl. Phys. Lett. **95**, 121101 (2009)

28. H. Nemec, P. Kuzel, F. Kadlec, C. Kadlec, R. Yahiaoui, P. Mounaix, Tunable terahertz metamaterials with negative permeability, Phys. Rev. B **79**, 241108 (2009)

29. M.S. Wheeler, J.S. Aitchison, J.I.L. Chen, G.A. Ozin, M. Mojahedi, Infrared magnetic response in a random silicon carbide micropowder, Phys. Rev. B **79**, 073103 (2009)

30. J.C. Ginn, I. Brener, D.W. Peters, J.R. Wendt, J.O. Stevens, P.F. Hines, L.I. Basilio, L.K. Warne, J.F. Ih-lefeld, P.G. Clem, M.B. Sinclair, Realizing optical magnetism from dielectric metamaterials, Phys. Rev. Lett. **108**, 097402 (2012)

31. J.A. Schuller, R. Zia, T. Taubner, M.L. Brongersma, Dielectric metamaterials based on electric and magnetic resonances of silicon carbide particles, Phys. Rev. Lett. **99**, 107401 (2007)

32. L. Shi, T.U. Tuzer, R. Fenollosa, F. Meseguer, A new dielectric metamaterial building block with a strong magnetic response in the sub-1.5-micrometer region: silicon colloid nanocavities, Adv. Mater. **24**, 5934 (2012)

33. N.I. Zheludev, Y.S. Kivshar, From metamaterials to metadevices, Nat. Mater. **11**, 917 (2012)

34. F. Gaufillet, S. Marcellin, E. Akmansoy, Dielectric meta-material-based gradient index lens in the terahertz frequency range, IEEE J. Sel. Top. Quantum Electron. **23**, 1 (2017)

35. N. Liu, H. Giessen, Coupling effects in optical meta-materials, Angew. Chem. In t. Ed. **49**, 9838 (2010)

36. F. Zhang, L. Kang, Q. Zhao, J. Zhou, D. Lip-pens, Magnetic and electric coupling effects of dielectric metamaterial, New J. Phys. **14**, 033031 (2012)

37. F. Zhang, V. Sadaune, L. Kang, Q. Zhao, J. Zhou, D. Lippens, Coupling effect for dielectric metamate-rial dimer, Prog. Electromagn. Res. **132**, 587 (2012)

38. S. Lanneb'ere, S. Campione, A. Aradian, M. Albani, F. Capolino, Artificial magnetism at terahertz frequencies from three-dimensional lattices of TiO_2 microspheres accounting for spatial dispersion and magnetoelectric coupling, J. Opt. Soc. Am. B **31**, 1078 (2014)

39. P. Albella, M.A. Poyli, M.K. Schmidt, S.A. Maier, F. Moreno, J.J. Śaenz, J. Aizpurua, Low-loss electric and magnetic field-enhanced spectroscopy with subwave-length silicon dimers, J. Phys. Chem. C **117**, 13573 (2013)

40. S. Marcellin, E. Akmansoy, Negative index and mode coupling in all-dielectric metamaterials at terahertz frequencies, in 2015 9th International Congress on Advanced Electromagnetic Materials in Microwaves and Optics (Metamaterials), Oxford, September 2015, pp. 4-6.

41. T. Lepetit, E. Akmansoy, J.-P. Ganne, Experimental evidence of resonant effective permittivity in a dielectric metamaterial, J. Appl. Phys. **109**, 023115 (2011)

42. N. Matsumoto, T. Hosokura, K. Kageyama, H. Takagi, Y. Sakabe, M. Hangyo, Analysis of dielectric response of TiO_2 in terahertz frequency region by general harmonic oscillator model, Jpn. J. Appl. Phys. **47**, 7725 (2008)

43. K. Berdel, J. Rivas, P. Bolivar, P. de Maagt, H. Kurz, Temperature dependence of the permittivity and loss tangent of high-permittivity materials at terahertz frequencies, IEEE Trans. Microw. Theory Tech. **53**, 1266 (2005)

44. R.A. Depine, A. Lakhtakia, A new condition to identify isotropic dielectric-magnetic materials displaying negative phase velocity, Microw. Opt. Tech. Lett. **41**, 315 (2004)

45. S.B. Cohn, Microwave bandpass filters containing high-q dielectric resonators, IEEE Trans. Microw. Theory Tech. **16**, 218 (1968)

46. J. Sethares, S. Naumann, Design of microwave dielectric resonators, IEEE Trans. Microw. Theory Tech. **MT14**, 2 (1966)

47. X. Chen, T.M. Grzegorczyk, B.-I. Wu, J. Pacheco, J.A. Kong, Robust method to retrieve the constitutive effective parameters of metamaterials, Phys. Rev. E **70**, 016608 (2004)

48. E. Prodan, C. Radloff, N.J. Halas, P. Nordlander, A hybridization model for the plasmon response of complex nanostructures, Science **302**, 5644 419 (2003)

49. H. Guo, N. Liu, L. Fu, T.P. Meyrath, T. Zentgraf, H. Schweizer, H. Giessen, Resonance hybridization in double split-ring resonator metamaterials, Opt. Express **15**, 12095 (2007)

50. R. Abdeddaim, A. Ourir, J. de Rosny, Realizing a negative index metamaterial by controlling hybridization of trapped modes, Phys. Rev. B **83**, 033101 (2011)

51. N.-H. Shen, L. Zhang, T. Koschny, B. Dastmalchi, M. Kafesaki, C.M. Soukoulis, Discontinuous design of negative index metamaterials based on mode hybridization, Appl. Phys. Lett. **101**, 081913 (2012)

52. N. Liu, H. Guo, L. Fu, S. Kaiser, H. Schweizer, H. Giessen, Plasmon hybridization in stacked cut-wire metamaterials, Adv. Mater. **19**, 3628 (2007)

53. A. Christ, O.J.F. Martin, Y. Ekinci, N.A. Gippius, S.G. Tikhodeev, Symmetry breaking in a plasmonic metamaterial at optical wavelength, Nano Lett. **8**, 2171 (2008)

54. B. Kanťe, Y.-S. Park, K. O'Brien, D. Shuldman, N.D. Lanzillotti-Kimura, Z. Jing Wong, X. Yin, X. Zhang, Symmetry breaking and optical negative index of closed nanorings, Nat. Commun. **3**, 1180 (2012)

55. P. Nordlander, C. Oubre, E. Prodan, K. Li, M.I. Stockman, Plasmon hybridization in nanoparticle dimers, Nano Lett. **4**, 899 (2004)

56. J. van de Groep, T. Coenen, S.A. Mann, A. Polman, Direct imaging of hybridized eigenmodes in coupled silicon nano-particles, Optica **3**, 93 (2016)

57. A.M. Nicolson, G.F. Ross, Measurement of the intrinsic properties of materials by time-domain techniques, IEEE Trans. Instrum. Meas. **19**, 377 (1970)

58. W. Weir, Automatic measurement of complex dielectric constant and permeability at microwave frequencies, Proc. IEEE **62**, 33 (1974)

59. Z. Szabo, G.H. Park, R. Hedge, E.P. Li, A unique extraction of metamaterial parameters based on Kramers-Kronig relation-ship, IEEE Trans. Microw. Theory Tech. **58**, 2646 (2010)

60. V. Varadan, R. Ro, Unique retrieval of complex permittivity and permeability of dispersive materials from reflection and transmitted fields by enforcing causality, IEEE Trans. Microw. Theory Tech. **55**, 2224 (2007)

61. D.R. Smith, S. Schultz, P. Markǒs, C.M. Soukoulis, Determination of effective permittivity and permeability of metamaterials from reflection and transmission coefficients, Phys. Rev. B **65**, 195104 (2002)

62. T. Koschny, P. Markǒs, D.R. Smith, C.M. Souk-oulis, Resonant and antiresonant frequency dependence of the effective parameters of metamaterials, Phys. Rev. E **68**, 065602 (2003)

63. D.R. Smith, D.C. Vier, T. Koschny, C.M. Souk-oulis, Electromagnetic parameter retrieval from inhomo-geneous metamaterials, Phys. Rev. E **71**, 036617 (2005)

64. A. Alú, Restoring the physical meaning of metamaterial constitutive parameters, Phys. Rev. B **83**, 081102 (2011)

65. C.R. Simovski, On electromagnetic characterization and homogenization of nanostructured metamaterials, J. Opt. **13**, 013001 (2011)

66. R.W. Ziolkowski, Propagation in and scattering from a matched metamaterial having a zero index of refraction, Phys. Rev. E **70**, 046608 (2004)

67. A. Alú, M.G. Silveirinha, A. Salandrino, N. En-gheta, Epsilon-near-zero metamaterials and electromagnetic sources: tailoring the radiation phase pattern, Phys. Rev. B **75**, 155410 (2007)

68. A. Sihvola, Metamaterials and depolarization factors, Prog. Electromagn. Res. 51, pp. 65–82, (2005)

69. W.G. Spitzer, R.C. Miller, D.A. Kleinman, L.E. Howarth, Far infrared dielectric dispersion in $BaTiO_3$, $SrTiO_3$, and TiO_2, Phys. Rev. **126**, 1710 (1962)

70. A.S. Barker, Temperature dependence of the transverse and longitudinal optic mode frequencies and charges in $srtio_3$ and $BaTiO_3$, Phys. Rev. **145**, 391 (1966)

71. J. Han, F. Wan, Z. Zhu, W. Zhang, Dielectric response of soft mode in ferroelectric $SrTiO_3$, Appl. Phys. Lett. **90**, 031104 (2007)

72. N. Matsumoto, T. Fujii, K. Kageyama, H. Takagi, T. Nagashima, M. Hangyo, Measurement of the soft-mode dispersion in $SrTiO_3$ by terahertz time-domain spectroscopic ellipsometry, Jpn. J. Appl. Phys. **48**, 09KC11 (2009)

73. F.M.C. Gervais, B. Piriou, Temperature dependence of transverse- and longitudinal-optic modes in TiO_2 (rutile), Phys. Rev. B **10**, 1642 (1974)

74. T. Tsurumi, J. Li, T. Hoshina, H. Kakemoto, M. Nakada, J. Akedo, Ultrawide range dielectric spectroscopy of BaTiO3-based perovskite dielectrics, Appl. Phys. Lett. **91**, 182905 (2007)

75. J. Petzelt, T. Ostapchuk, I. Gregora, I. Rychetský, S. Hoffmann-Eifert, A.V. Pronin, Y. Yuzyuk, B.P. Gorshunov, S. Kamba, V. Bovtun, J. Pokorný, M. Savinov, V. Porokhonskyy, D. Rafaja, P. Vaňek, A. Almeida, M.R. Chaves, A.A. Volkov, M. Dressel, R. Waser, Dielectric, infrared, and Raman response of undoped $SrTiO_3$ ceramics: evidence of polar grain boundaries, Phys. Rev. B **64**, 184111 (2001)